This article has been accepted for inclusion in a future issue of this journal. Content is final as presented, with the exception of pagination.

Recombination Analysis of Phosphorus-Doped Nanostructured Silicon Oxide Passivating Electron Contacts for Silicon Solar Cells

Josua Stuckelberger, Gizem Nogay, Philippe Wyss, Andrea Ingenito, Christophe Allebé, Jörg Horzel, Brett A. Kamino, Matthieu Despeisse, Franz-Josef Haug, Philipp Löper, and Christophe Ballif

***Abstract*—We analyze the recombination properties of passivating electron selective contacts based on nanostructured silicon oxide. Our contact design is based on an interfacial buffer oxide capped with a bilayer structure of phosphorus-doped silicon oxide and silicon which is annealed at 900 °C. We investigate in detail the effects of the initial dopant concentration in the bilayer and of the anneal dwell time on dopant in-diffusion, contact formation, and interface recombination. Our investigation addresses also the hydrogenation of interface defects and the effect of indium-tin-oxide (ITO) sputtering, allowing us to separate the interplay between enhanced field-effect passivation, Auger recombination, and interface recombination. After thermal annealing, the passivating electron selective contact presented here attains a saturation current density (J_0) of 12.4 fA cm^{-2} for medium doping, which improves further upon hydrogenation to $J_0 = 8.1$ fA cm^{-2}. For specific contact resistances <500 mΩ cm^2, however, higher doping concentrations are required. For those doping concentrations, the saturation current density is 13.9 fA cm^{-2} and increases by 10% upon sputter-deposition of an ITO layer on top of the electron selective stack.**

***Index Terms*—Chemical oxide, contact resistivity, EDNA 2, indium-tin-oxide (ITO) sputtering, mixed-phase, passivating contact, phosphorus diffusion, silicon, silicon solar cells, SiOx, surface recombination velocity (SRV).**

Manuscript received September 15, 2017; revised November 3, 2017; accepted November 21, 2017. This work was supported in part by the Swiss National Science Foundation under Grant 200021_14588/1 and Grant IZLIZ2_156641, in part by the Swiss Federal Office for Energy under Grant SI/501253-01, and in part by the European Commission in the project Horizon 2020 under Grant 727529. *(Corresponding author: Josua Stuckelberger.)*

J. Stuckelberger, G. Nogay, P. Wyss, A. Ingenito, F.-J. Haug, and P. Löper are with the Photovoltaics and Thin-Film Electronics Laboratory, Institute of Microengineering, École Polytechnique Fédérale de Lausanne, Neuchâtel 2002, Switzerland (e-mail: josua.stuckelberger@epfl.ch; gizem.nogay@epfl.ch; philippe.wyss@epfl.ch; andrea.ingenito@epfl.ch; franz-josef.haug@epfl.ch; philipp.loeper@epfl.ch).

C. Allebé, J. Horzel, B. A. Kamino, and M. Despeisse are with the Swiss Center for Electronics and Microtechnology, Neuchâtel 2002, Switzerland (e-mail: Christophe.ALLEBE@csem.ch; Joerg.HORZEL@csem.ch; brett.kamino@csem.ch; matthieu.despeisse@csem.ch).

C. Ballif is with the Photovoltaics and Thin-Film Electronics Laboratory, Institute of Microengineering, École Polytechnique Fédérale de Lausanne, Neuchâtel 2002, Switzerland, and also with the Swiss Center for Electronics and Microtechnology, Neuchâtel 2002, Switzerland (e-mail: christophe.ballif@epfl.ch).

Color versions of one or more of the figures in this paper are available online at http://ieeexplore.ieee.org.

Digital Object Identifier 10.1109/JPHOTOV.2017.2779871

I. Introduction

The main limitation of industrial high-efficiency crystalline silicon (c-Si) solar cells with direct metal/silicon contacts is a high charge carrier recombination rate at the metal interface [1]. To overcome the ensuing voltage loss, novel passivation- and contact-schemes are required. First, approaches to passivate the silicon wafer by a thin silicon oxide layer capped with doped poly-silicon were pioneered already in the 1980s [2]–[4]. Instead of using pure poly-Si layers, impressive passivation was obtained with a variant of those approaches using semi-insulating poly-Si (SIPOS), which were alloyed with oxygen, but the films were too resistive for extraction of current from solar cells [3]–[5]. Recently, impressive solar cell results were demonstrated using a similar approach, mainly on the rear side for both-sided contacted solar cells and interdigitated back contacted (IBC) devices without alloying with oxygen [6]–[12], but all these structures have in common that a highly doped surface region is formed within the wafer by in-diffusion of dopants from the deposited layer during a thermal annealing step. This highly doped surface region supports the charge carrier selectivity of the contact [13]. Additionally, most structures benefit from a hydrogenation step, which is usually explained with a reduction of the electronic defect density at the wafer/SiO_X interface or in the layer stack [14].

When such a passivating rear contact is employed, the recombination loss at the front side metallization becomes the efficiency limiting element [15]. To mitigate this loss, we recently presented a novel full-area passivating electron contact which targets enhanced transparency by replacing a part of the doped Si-layer by SiO_X [16]. This novel contact structure consists of a thin SiO_X layer grown chemically (chem-SiO_X) on the c-Si wafer surface, capped by a phosphorus-doped mixed-phase silicon oxide (mp-SiO_X) layer and a nanocrystalline silicon (nc-Si) layer. Compared with the SIPOS structure, the mp-SiO_X used in this contribution has higher oxygen content, but it contains Si filaments in the direction of growth that support transverse conductivity. The filaments are a result of using appropriate growth conditions during plasma-enhanced chemical vapor deposition (PECVD) [17]. Analysis with transmission electron microscopy reveals that those Si filaments, embedded in an SiO_X matrix, extend through the layer, with increasing Si concentration and crystallinity toward its top interface in the "as-deposited" state as well as after the annealing [16]. Moreover, the presence of SiO_X enhances the temperature stability of the passivation, resulting in a broad thermal processing window. In a preceding

2156-3381 © 2018 IEEE. Personal use is permitted, but republication/redistribution requires IEEE permission.
See http://www.ieee.org/publications_standards/publications/rights/index.html for more information.

This article has been accepted for inclusion in a future issue of this journal. Content is final as presented, with the exception of pagination.

publication [16], a high concentration of phosphorus at the interface between the wafer and the chem-SiO_X/mp-SiO_X/nc-Si layer stack was reported, causing Auger recombination and thus imposing a lower limit of the emitter saturation current density (J_0).

In this paper, we investigate further the interplay between enhanced screening of minority carriers, Auger recombination, and interface recombination, which all increase monotonically with surface concentration [18]–[20]. Whereas a higher doping concentration leads to an increase in Auger recombination [21], it also increases the density of majority carriers (electrons) and consequently decreases the density of minority carriers (holes) at the interface [22]. On the other hand, dopant diffusion through the SiO_X into the wafer can also cause electrical defects at the wafer/chemical SiO_X interface as reported for boron diffusion [23]. These can be partially passivated by an additional hydrogenation step [14].

By varying the annealing time and initial doping concentrations of the deposited stacks, the junction properties are analyzed and the influence of the individual effects are separated by investigations before and after hydrogen passivation in a forming gas anneal (FGA). Additionally, we apply an electrode of sputtered indium-tin-oxide (ITO) in order to finalize a solar cell structure and to study possible effects on passivation quality for samples dominated by the different recombination behavior.

II. Experimental

The passivating electron selective contact was investigated on planar symmetrical test structures based on 200 μm thick 4-inch <100>-oriented 10 Ω cm phosphorus-doped n-type FZ silicon wafers. After standard wet chemical cleaning, a ~1.2 nm thin SiO_X layer was grown by wet chemical oxidation in an azeotropic HNO_3 solution [24], [25], referred to as "chemical SiO_X" (chem-SiO_X hereafter). Subsequently, both sides were covered with the mp-SiO_X/nc-Si bilayer structure, using thicknesses of ~12 and ~17 nm, respectively. The films were deposited by PECVD using SiH_4, H_2, CO_2 as reported in more detail in [16], and PH_3 was added for *in situ* phosphorus-doping. In the following, PECVD-deposited layers are referred to as mp-SiO_X and nc-Si in order to distinguish them from the chem-SiO_X. The initial doping concentrations of both layers were varied during this experiment, using four different phosphine (PH_3) flow rates. The samples were then annealed in nitrogen (N_2) at 900 °C for four different dwell times, namely 15, 30, 60, and 90 min, resulting in different surface concentrations and doping profiles. The annealing was followed by a 30 min forming gas anneal (FGA, 4% H_2 in N_2) at 500 °C to passivate electronic defects at the c-Si/chem-SiO_X interface. The samples were dipped in a diluted hydrofluoric acid (HF) solution (1 vol.-%) until the surfaces became hydrophobic prior to sputtering ITO on both sides. The samples were subsequently cured at 210 °C for 30 min. The effective minority carrier lifetime was measured by photo-conductance decay (PCD) applying the method of Kimmerle [26] to extract the emitter saturation current density J_0 at an excess carrier density corresponding to ten times the base doping. The error in this J_0 measurement including inhomogeneity over the wafer area is smaller than 10%. The spatial homogeneity of the passivation was analyzed using photoluminescence imaging. The electrically active phosphorus doping profile diffused into the c-Si was measured by electrochemical-capacitance-voltage (ECV) measurements using 0.1 molar ammonium hydrogen difluoride (NH_4HF_2) solution after stripping the whole layer stack by prolonged etching in a 20 vol.-% HF solution. The software EDNA 2 [27] was used to simulate the saturation current density for the measured doping profiles as a function of the surface recombination velocity (SRV) at the wafer/layer stack interface. We used the inverse function $\mathrm{SRV}(J_0)$ to determine the SRV value for the corresponding J_0 value determined by PCD. The contact resistivity was measured by the transfer length method (TLM) on coplanar contact pads deposited on the mp-SiO_X/nc-Si layer stack after the FGA. We used two types of contact, either evaporated aluminum (Al) or sputtered ITO covered by silver paste, and the layer stack was not etched back between the contact pads since the influence of the layer on the contact resistivity is negligible for this contact structure as reported in [16].

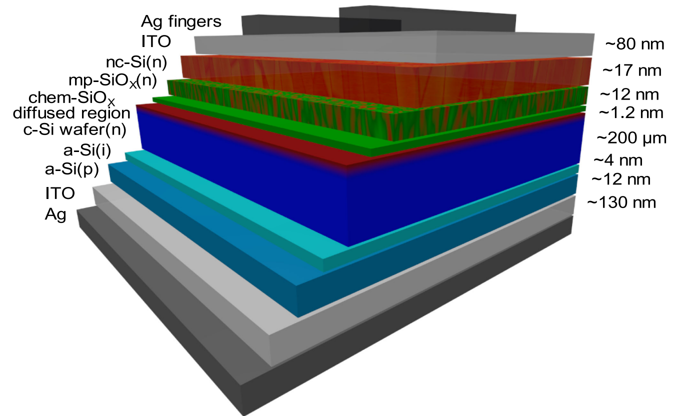

Fig. 1. Sketch of the layer stack employed in the proof-of-concept solar cell.

For the proof-of-concept solar cells, we prepared first the passivating electron contact on the front side of a planar <100>-oriented 1 Ω cm phosphorus-doped 200 μm thick n-type silicon wafer. Then, we applied a silicon heterojunction (SHJ) hole selective contact to the rear side applying subsequently thin intrinsic amorphous silicon (a-Si:H) and boron-doped a-Si:H(p) layers. After an HF dip, ITO was sputtered on front and rear through 2.2 × 2.2 cm^2 shadow masks that were aligned to cover the same area. Different from lifetime samples, thicknesses of 80 and 130 nm were used for front and rear side of the solar cells, respectively. The solar cells were then finished by sputtering a silver reflector on the rear side and screen printing an Ag grid on the front side, followed by curing for 30 min at 210 °C in a belt furnace. A sketch of the final layer stack of our device is illustrated in Fig. 1 and more detailed information about the fabrication process for the hybrid cells can be found elsewhere [28]. Current voltage (*I–V*) characteristics of the cells were measured at 25 °C with a source meter (Keithley, 2601A), using an AAA solar simulator (Wacom) calibrated to 100 mW cm^{-2} with a c-Si reference cell. $\mathrm{Suns}-V_{\mathrm{OC}}$ measurements were carried out on the individual cells at 25 °C using the $\mathrm{Suns}-V_{\mathrm{OC}}$ unit of a WCT-100 photoconductance tool by Sinton Consulting Inc. The external quantum efficiency (EQE) was measured between the metal fingers by an in-house build system calibrated with a certified SHJ cell. Together with the reflectance (R) measured in a Perkin-Elmer Lambda 950 spectrometer, the internal quantum efficiency (IQE) was calculated.

This article has been accepted for inclusion in a future issue of this journal. Content is final as presented, with the exception of pagination.

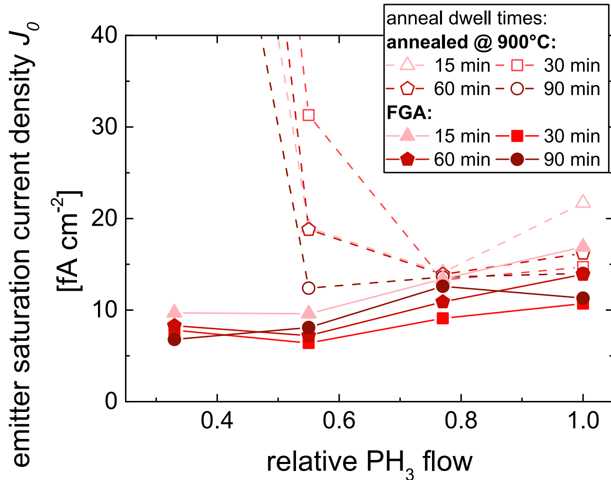

Fig. 2. Emitter saturation current density J_0 as a function of the relative PH_3 flow used during PECVD deposition for four different anneal dwell times directly after the anneal (dashed lines, open symbols) and after a hydrogenation by FGA (lines, filled symbols).

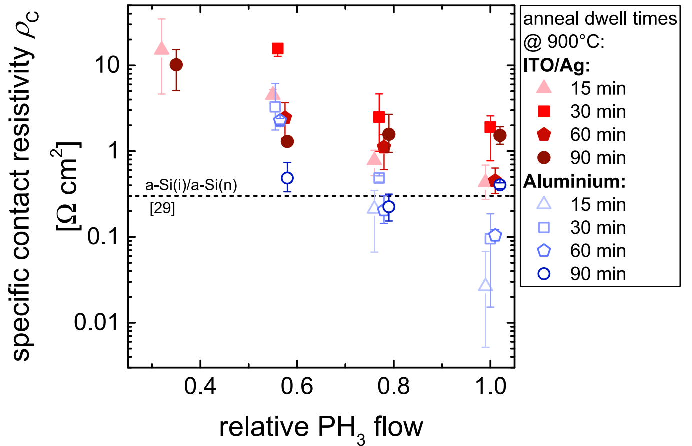

Fig. 3. Specific contact resistivity ρ_c as a function of the relative PH_3 flow used during PECVD deposition for four different anneal dwell times extracted from TLM measurements using ITO/Ag (red filled symbols) or aluminum (blue open symbols) as metallization. The data points are moved slightly in the horizontal direction for better readability.

III. Results and Discussion

A. Surface Passivation

Fig. 2 shows the measured emitter saturation current density (J_0) as a function of relative PH_3 flow during deposition (maximal used PH_3 flow is set to 1) after applying four different anneal dwell times at 900 °C. The J_0 is measured directly after the annealing process and then again after the FGA. The open symbols show that even without the FGA, remarkably good passivation with J_0 values below 20 fA cm^{-2} can be attained for the higher PH_3 flows. For short dwell times of 15 and 30 min, a relative flow of 0.77 during deposition leads to best passivation. For longer dwell times, on the other hand, a relative flow of 0.56 shows the best behavior, leading to a value of $J_0 = 12.4$ fA cm^{-2}.

Full symbols show that the FGA is especially effective to improve J_0 of samples with low phosphine flow, suggesting that their behavior is dominated by defects at the chem-SiO_X/wafer interface. With FGA, the optimum is reached for a relative PH_3 flow of 0.56 and a dwell time of 30 min, resulting in $J_0 = 6.4$ fA cm^{-2}.

Samples with high phosphine flows are insensitive to FGA, suggesting that the overall recombination rate is dominated by the in-diffused region which is little affected by hydrogenation. The increase of J_0 for relative flows higher than 0.56 (after FGA) can be explained with an increasing contribution from Auger recombination.

These results show different pathways to improve surface passivation, either by low initial doping concentrations combined with long annealing and hydrogenation or high initial doping concentrations, for which a short annealing dwell time is sufficient and an FGA is not necessary.

B. Electrical Characterization

The specific contact resistivity ρ_C for this sample series is shown in Fig. 3 as a function of relative PH_3 flow and for the four different anneal dwell times at 900 °C before metallization. Error bars denote the average over three TLM samples prepared for each condition. For both contact types, high doping is needed for low contact resistivity, but evaporated aluminum (blue open symbols) yields lower values than sputtered ITO with silver paste (ITO/Ag, red filled symbols).

For low doping of 0.33 relative PH_3 flow, the samples were hardly measurable giving ρ_C values of above 5 Ω cm^2. For a relative PH_3 flow of 0.56, ρ_C is decreasing with longer anneal dwell time and only for 90 min anneal and contacting with aluminum ρ_C gets below 500 mΩ cm^2. For a relative PH_3 flow of 0.77, ρ_C is not following a trend with anneal dwell time, only a clear beneficial behavior of aluminum over ITO/Ag is observed leading to ρ_C of $\sim$200 mΩ cm^2. For comparison, the contact resistivity of a-Si(i)/a-Si(n) SHJ contacts (see the dashed line in Fig. 3) is reported to be ca. 300 mΩ cm^2 [29]. For a higher relative PH_3 flow of 1.00, ρ_C with ITO is also below 500 mΩ cm^2 for some conditions. Using aluminum, ρ_C is lower for shorter anneal dwell time with an optimum at 15 min, leading to an average ρ_C of 26 mΩ cm^2. An explanation for the lower ρ_C for Al compared with ITO could be a difference in their work function. For ITO, the work function varies with stoichiometry, organic contamination, and oxidation type [30], [31]. A higher effective barrier for ITO would broaden the depletion region and lead to a decrease in tunnel probability, which is the dominant term in our Schottky contact due to the high doping concentration in silicon [32]. On the other hand, due to Fermi level pinning, the exact effect of the work function is hard to predict [33]. Additionally, the presence of oxygen during the ITO sputtering could lead to a thin SiO_X layer between the silicon and the ITO, acting as additional barrier.

As can be seen from the error bars, the samples with ITO should be treated with caution and are reported here to give a more complete picture and to show that a charge carrier transport with low ρ_C is possible through this mixed-phase SiO_X layer stack, but only by using higher doping concentrations. Since a J_0 value < 10 fA cm^{-2} should be sufficient for most applications in high-efficiency solar cells, these higher PH_3 flows needed for a good electrical transport can be applied.

This article has been accepted for inclusion in a future issue of this journal. Content is final as presented, with the exception of pagination.

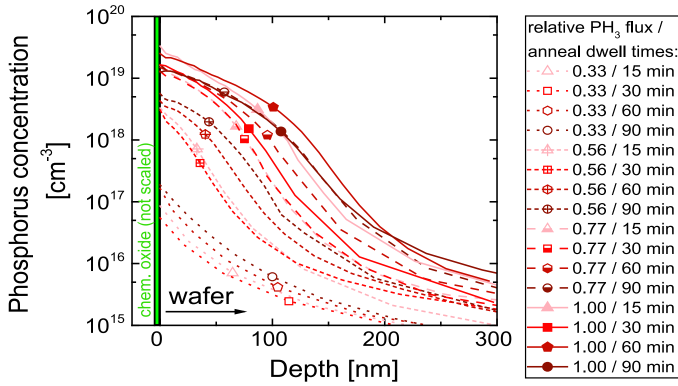

Fig. 4. Phosphorus doping profiles measured by ECV in the c-Si wafer after etching off the deposited layer stacks.

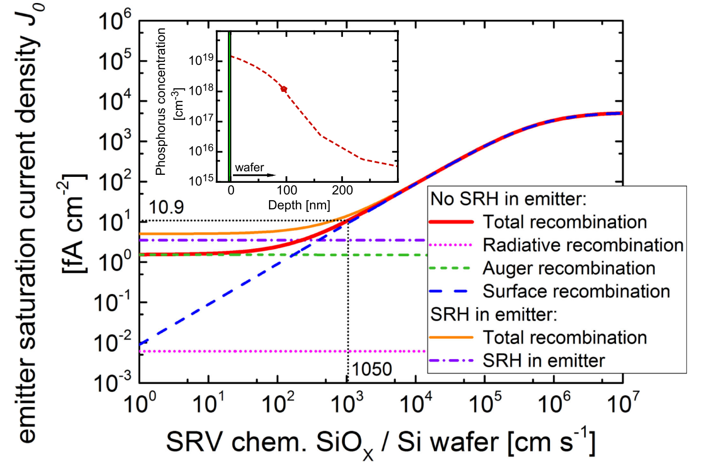

Fig. 5. Total J_0 as a function of SRV at the chem.SiO$_X$/wafer interface for the example of a relative PH$_3$ flow of 0.77 and an anneal dwell time of 60 min (doping profile shown as inset). The contribution of radiative (purple), Auger (green), and surface (blue) recombination to the total J_0 (red) are indicated. The effect of SRH in the emitter (violet) leads to a different total J_0 (orange). In dotted black lines the measured J_0 after FGA and the corresponding SRV is marked.

C. Doping Profiles

The doping profiles of our sample set after FGA are shown in Fig. 4. There are roughly three groups which are distinguished primarily by low, medium, and high PH$_3$ flow. The dwell times give rise to only minor differences within the groups. A relative flow of 0.33 results in a comparatively shallow profile for all anneal dwell times, whereas a relative flow of 0.56 already increases the surface concentration by more than one order of magnitude. For 0.77 and 1.00 relative PH$_3$ flow, the doping profiles are on a similar level, but it should be noted that the profiles were measured by ECV which only detects electrically active dopant atoms.

D. EDNA 2 Simulations

The doping profiles shown in Fig. 4 were used to simulate J_0 as a function of SRV at the wafer/layer stack interface using EDNA 2 [27]. This SRV thus lumps all recombination processes occurring at the interface between the wafer and the deposited layer stack and within the layer stack, independently of their exact mechanism. Fig. 5 resolves the individual contributions illustrated for the doping profile (inset) of the sample with 0.77 relative PH$_3$ flow and an anneal of 60 min at 900 °C. Radiative recombination (purple) is taken into account according to the model of Trupke [34], Auger recombination (green) is treated with the model described by Richter in [35, Table II], giving a lower threshold for J_0 at low SRV, and surface recombination (blue) is determined by $U_{\mathrm{surf}} = \mathrm{SRV} \cdot \Delta n$, with the recombination rate U_{surf} and the excess carrier concentration Δn. Based on the experimentally determined J_0 of 10.9 fA cm^{-2} after FGA, an SRV of 1050 cm^{-1} is read off the characteristic.

For simplicity, we assume zero surface charge and no Shockley–Read–Hall (SRH) recombination in the bulk of the emitter because the material used was of high quality and the measured P concentrations are more than one order of magnitude lower than the solubility limit given by Solmi [36]. Note that this assumption leads to an upper limit for the SRV derived on the basis of the measured J_0. To further justify our assumption, we projected a worst-case scenario in Fig. 5 using the assumptions $\tau_{n0} = 5000\,\mu$s, $\tau_{p0} = 1\,\mu$s and $E_{\mathrm{t}} - E_{\mathrm{i}} = 0.3$ eV to illustrate the effect of SRH recombination in the emitter (violet), leading to a different total $J_0\,(\mathrm{orange})$. This would result in an SRV of 657 cm s^{-1} (intersection with orange curve) instead of SRV 1050 cm s^{-1} (intersection with red curve).

The simulations for the ECV doping profiles of all 16 samples are summarized in Fig. 6. The symbols overlaid on the curves refer to the experimentally determined values of J_0 after FGA. For low phosphorus concentrations (relative PH$_3$ flow of 0.33) the dependence of J_0 on SRV (straight line in the log–log plot) is approximately described by a power-law over almost the whole SRV range. This trend indicates that on one hand it is possible to reach very low J_0 values for very low SRV, but on the other hand, the contact is very sensitive to the amount of interface recombination.

By increasing the doping to a relative PH$_3$ flow of 0.56, the lowest reachable J_0 values extend into a similar range, but they are less sensitive to SRV values between 1 and 50 cm s^{-1}. Fig. 4 showed that this condition yields a deeper in-diffused region, resulting in reduction of the minority hole concentration close to the interface between chem-SiO$_X$ and wafer and thus a lower recombination rate at this interface.

For even higher relative PH$_3$ flows of 0.77 and 1.00, the minimal attainable J_0 for low SRV is clearly increased up to values between 1 and 4 fA cm^{-2} due to Auger recombination, but at the same time, J_0 is more robust against variation of SRV. As Fig. 6 depicts, J_0 stays almost constant until around 1000 cm^{-1} before the monomial behavior arises.

For SRV in the range between 10^3 and 10^5 cm s^{-1}, in which all curves show monomial behavior, higher doping concentrations result in lower J_0 values. All lie in the range of 100–1000 cm s^{-1}, giving the possibility to use higher doping concentrations without being limited by Auger recombination.

E. Surface Recombination

We determined the SRV of all of our structures from the simulated $J_0(\mathrm{SRV})$ dependence and the experimentally determined J_0 values. Additionally, we measured J_0 after sputtering of ITO electrodes and once more after curing. Fig. 7 depicts the extracted SRV values as a function of the phosphorus concentration at the wafer surface (N_{dop}). Note that even with a relative error of 10% in J_0, almost all error bars for the resulting SRV are smaller

This article has been accepted for inclusion in a future issue of this journal. Content is final as presented, with the exception of pagination.

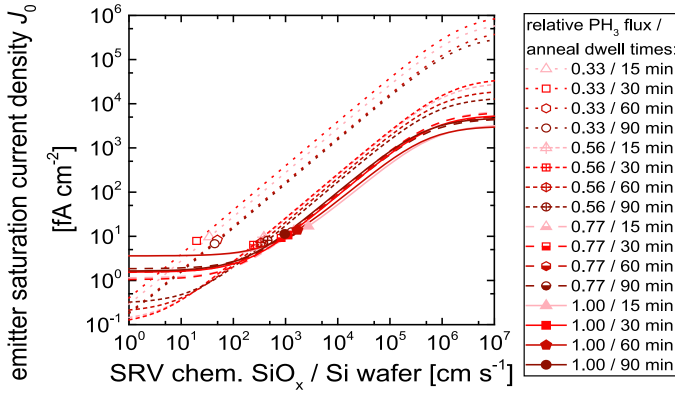

Fig. 6. Simulations for J_0 as a function of SRV at the chem. SiO_X/wafer interface out of doping profiles shown in Fig. 4 processed by EDNA 2 [27].

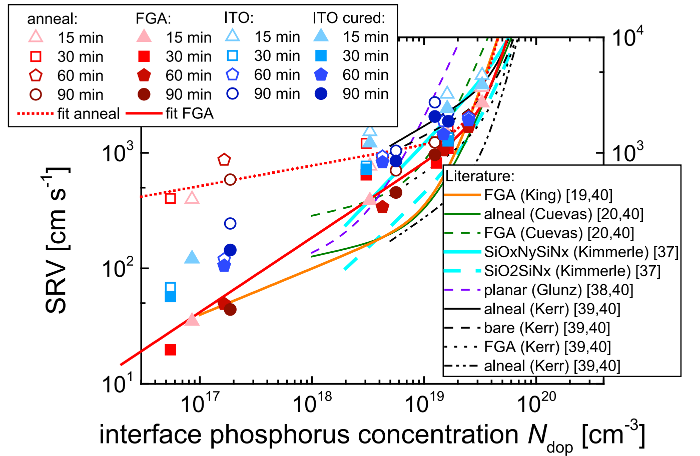

Fig. 7. Extracted SRV values from the combination of measured J_0 and the simulations out of doping profiles plotted versus the phosphorus concentration at the chem.SiO_X/wafer interface. The values are compared with literature data for dielectric passivation layers.

than the symbol size, so they are not plotted. Before FGA (red open symbols) the SRV for low N_{dop}, $5 \cdot 10^{16} - 2 \cdot 10^{17}$ cm^{-3}, and high N_{dop}, $1 - 4 \cdot 10^{19}$ cm^{-3}, lie between 400 (low N_{dop}) and 3700 cm s^{-1} (high N_{dop}). After FGA (red filled symbols), the SRV of those with low N_{dop} improve by a factor of up to 20 to values as low as 20 cm s^{-1}, whereas for high N_{dop} the SRV improve only by a factor of 1–1.5.

In Fig. 7, we have also replotted literature data for SiO_2 and SiO_X/SiN_Y passivation layers [19], [20], [37]–[40]. Note that these layers were dielectric layers, and did not work as charge carrier extraction layers. Fig. 7 shows that the SRV of our passivating electron contact follows a very similar dependence on N_{dop}. Following [40] we describe the dependence of SRV on the interface phosphorus concentration by the following equation [40]:

$$\mathrm{SRV} = S_{\mathrm{p1}}\left(\frac{N_{\mathrm{dop}}}{10^{19}\mathrm{cm}^{-3}}\right)^{\gamma_1} + S_{\mathrm{p2}}\left(\frac{N_{\mathrm{dop}}}{10^{19}\mathrm{cm}^{-3}}\right)^{\gamma_2} \quad (1)$$

using the fit parameters S_{p1}, S_{p2}, γ_1, and γ_2. Due to the lack of data at high N_{dop} the second term is rather uncertain and γ_2 is therefore set to 4 as used by [40] to parametrize the data of [39]. The found parametrizations for the mp-SiO_X/nc-Si layer stack after anneal and after FGA are summarized in Table I and compared with the parametrizations reported for a dielectric thermal silicon oxide before and after an FGA [39], [40]. Whereas the exponent γ_1 is clearly lower for the chem-SiO_X/mp-SiO_X/nc-Si samples without FGA compared with the reported samples with bare oxide, this fit parameter γ_1 is very similar when comparing after the FGA.

The dielectric passivation layers [19], [20], [37]–[40] are electrically insulating and thus do not allow the establishment of an electrical contact for charge carrier extraction. The passivating contact layer stack presented here shows a very similar dependence of SRV over the studied surface phosphorus concentration range and in addition, this layer stack also acts as electrical contact to the silicon wafer, thanks to the silicon inclusions as was shown in [16].

Fig. 8 shows J_0 (left axis) at the different steps of contact formation, grouped by the relative PH_3 flow. The crosshatched area at the top of the bars represents the contribution of Auger recombination, extracted from the EDNA 2 simulations as described in Section III-D. Low PH_3 flows and short anneal dwell times result in shallow doping profiles and therefore low Auger recombination. These conditions yield the lowest J_0 values after

TABLE I
PARAMETERS IN (1) TO APPROXIMATE SRV VALUES SHOWN IN FIG. 7

	S_{p1} [cm s^{-1}]	γ_1	S_{p2} [cm s^{-1}]	γ_2
mp-SiO_X/nc-Si (after anneal)	1165	0.18	19.0	4
mp-SiO_X/nc-Si (FGA)	816	0.65	7.7	4
thermal SiO_2 [39], [40]	1400	0.5	4	4
thermal SiO_2 (FGA) [39], [40]	670	0.65	4	4

FGA. For longer dwell times and increasing doping levels, J_0 generally increases due to increasing Auger recombination. Additionally, the diffusion of a larger amount of dopants through the chemical oxide can also create defects and hence additional recombination centers at the interface.

Sputtering of ITO increases J_0 in all cases, but it is particularly detrimental for the J_0 of samples with low relative PH_3 flows of 0.33 and 0.56. These conditions coincide with low surface phosphorus concentrations in the range of 10^{16}–10^{17} cm^{-3}. In Fig. 7, the corresponding samples showed the largest improvements by FGA (reduction of their SRVs by a factor of up to 20), but also larger sensitivity to loss of interface passivation (increase of SRV after ITO sputtering by a factor of ∼3–5). Samples with higher relative phosphorus flow of 0.77 and 1.00 are more resilient against ITO sputtering damage. Consequently, they are more promising for device fabrication despite their higher contribution of Auger recombination.

For heterojunction solar cells, it was reported that the detrimental losses of ITO sputtering can be regained by curing [41], [42]. This effect is also visible for our passivating electron contact, but the SRV shown in Fig. 7 is reduced only by a factor of 1–1.5, and rather independently of the phosphorus surface concentration as shown by the filled blue symbols in Fig. 7, indicating that sputtering induced damage cannot be fully recovered. This leads to SRV values after curing between 50 and 150 cm s^{-1} for N_{dop} of 10^{16}–10^{17} cm^{-3}. For N_{dop} in the range of 10^{18} cm^{-3} SRV ranges between 700 and 1200 cm s^{-1}. For still higher N_{dop}, an SRV in the range of 1500–4000 cm s^{-1} is extracted. The influence of the curing (after ITO deposition) is

This article has been accepted for inclusion in a future issue of this journal. Content is final as presented, with the exception of pagination.

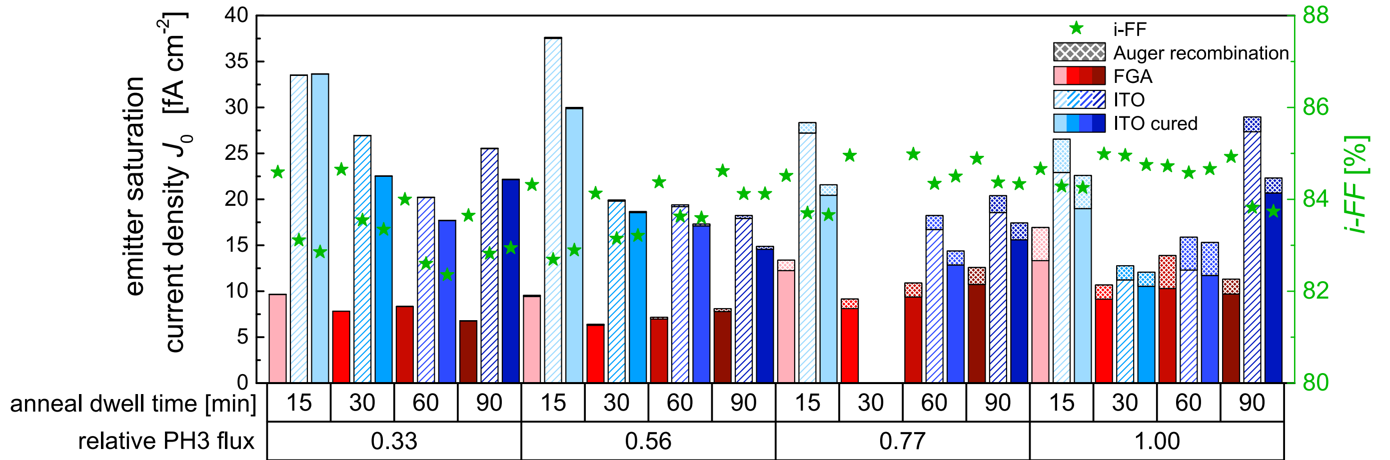

Fig. 8. Emitter saturation current density J_0 and its evolution after FGA (red), after ITO sputtering (blue striped) and its curing (blue filled) as a function of the relative PH_3 flow and the anneal dwell time. The contribution of Auger recombination to each J_0 is marked crosshatched. The *i-FF* (green stars, right axis) shows the influence of the ITO deposition at maximal-power-point (mpp) conditions.

also shown in Fig. 8, and for most samples it is on a similar level.

Conditions with higher relative PH_3 flows and longer anneal times lead to several conditions with a J_0 below 15 fA cm^{-2}. The optimum in our dataset is found at a relative PH_3 flow of 1.00 and a dwell time of 30 min, resulting in a J_0 of 12.1 fA cm^{-2}. Therein, Auger recombination contributes 1.5 fA cm^{-2}.

A closer look at the impact of ITO (including the curing) on the passivation clearly shows a stronger impact on samples with low interface concentrations for which chemical passivation plays a dominant role to reach high surface passivation. It is remarkable that even though some of the conditions used have rather high interface concentrations of $2.5 \cdot 10^{19}$ cm^{-3}, the resulting contribution of Auger recombination to J_0 was found to be < 3.6 fA cm^{-2} and has therefore a lower impact on the final performance than the ITO sputtering.

We also report the implied fill factor (*i-FF*) in Fig. 8 (green stars, right axis) in order to show the influence of the ITO deposition at maximal-power-point conditions. The same trend as for J_0 is observed: The degradation is stronger (losses of up to 1.75% absolute) for low doping, and the *i-FF* does not recover by curing, whereas for the best condition with a relative PH_3 flow of 1.00 annealed for 30 min, the *i-FF* drops only by 0.25% from 85.0% to 84.75%.

We assume that the doping profile and therefore the Auger recombination is not affected by the ITO sputtering. Therefore, this higher impact on samples with low interface concentrations could be related to a degradation of the chemical passivation due to sputtering and/or to the detrimental effect of band bending induced by the work function of the ITO, effectively reducing the electron concentration at the Si surface, an effect already reported for heterojunction solar cells [43], [44].

F. Proof-of-Concept Solar Cells

As a proof-of-concept and to further investigate this mixed-phase SiO_X layer stack, a hybrid solar cell (SHJ rear side) was fabricated on a *planar* 1 Ω cm phosphorus-doped n-type wafer having ITO/Ag as metallization. To this end, the condition giving the lowest ρ_C with a relative PH_3 flow of 1.00 and anneal dwell time of 15 min was chosen, no FGA was applied. Fig. 9 depicts the measured *J-V* curve under illumination (blue) together with the Suns $- V_{OC}$ measurement (dashed red). A fill factor *(FF)* of 79.4% demonstrates efficient carrier transport through the mixed-phase layer with a series resistance R_S of 0.19 Ω cm^2 extracted by the method of Wolf [45], [46]. The short-circuit current density (J_{SC}) of 33.9 mA cm^{-2} is promising for a planar solar cell compared with an upper limit of 35.7 mA cm^{-2} simulated with Wafer ray tracer [47] for a planar ideal device using nitride/wafer/nitride/Ag on a 200 μm wafer including the same shading losses of 5%. The high J_{SC} shows the potential of this contact as a front layer even though the open-circuit voltage (V_{OC}) of 691 mV is lower than expected. We relate the low V_{oc} to several not optimized cell fabrication steps, especially on wafer surface conditioning before the SHJ rear side deposition, since the lifetime after the rear side deposition is only improving slightly. We also assume this to be the reason for the low pseudo *FF* (*p-FF*) of only 83.0%, since on symmetrical samples with a-Si(i)/a-Si(p), using the same fabrication method as for the proof-of-concept cell, an *i-FF* of only 78.4% was observed before the ITO deposition. Nevertheless, the *planar* proof-of-concept device shown in Fig. 9 has a conversion efficiency η of 18.6%.

In Fig. 10, the EQE of the planar proof-of-concept solar cell is plotted together with the reflectance (R) and the calculated IQE in comparison with a planar SHJ cell (dashed lines) in rear emitter configuration (all EQEs are measured between the contact fingers). Both cells have an a-Si(i)/a-Si(p) rear contact, but the contacts were not codeposited, and the flat SHJ cell was fabricated on a 270 μm thick n-type wafer, thus explaining the differences at long wavelengths. At short wavelengths, the differences visible in EQE and R are mainly determined by the front layer, allowing a direct comparison of our mp-SiO_X(n)/nc-Si(n) layer stack (∼12/∼17 nm) with the SHJ a-Si(i)/a-Si(n) front (∼4/∼6 nm). Below 400 nm, the EQE response of the proof-of-concept cell is lower than the SHJ. This could be related to parasitic absorption which is lower for a-Si than for nc-Si in this range. Between 400 and 550 nm, the proof-of-concept cell shows a strong increase in EQE as well as IQE which is associated to the low parasitic absorption in the front mp-SiO_X(n)/nc-Si(n) layer stack as well as low reflectance. Above 550 nm, the IQE of the proof-of-concept

This article has been accepted for inclusion in a future issue of this journal. Content is final as presented, with the exception of pagination.

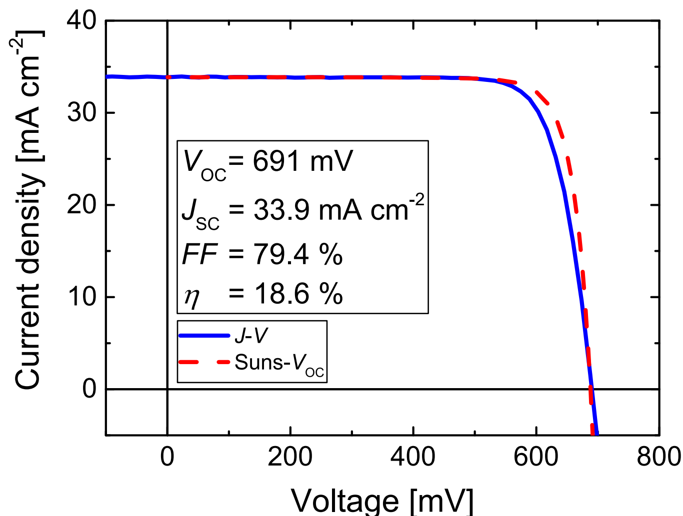

Fig. 9. *J–V* characteristics of a planar hybrid cell with the mixed-phase SiO_X layer n-type stack at the front and an amorphous heterojunction p-type hole collector at the rear.

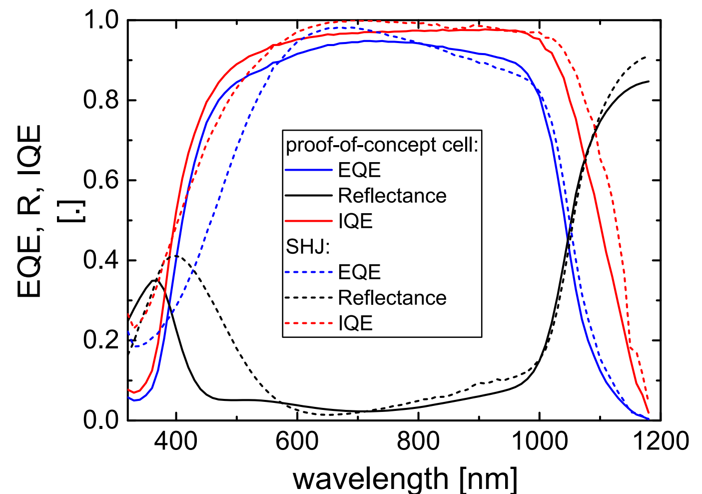

Fig. 10. EQE, reflectance, and IQE of the proof-of-concept solar cell in comparison with a planar SHJ cell. Both cells are realized with an n-type wafer in rear emitter configuration.

cells remains below 97%, indicating recombination losses at the front side.

An interesting additional feature of the proof-of-concept cell is visible in R. For a broad wavelength (λ) range of 450 nm $< \lambda <$ 950 nm, R is below 10% showing an antireflection behavior of the mp-SiO_X (n)/nc-Si(n) layer stack at the front, even though the ITO thickness is not optimized yet. We, therefore, assume that the effective refractive index of the mp-SiO_X (n)/Si(n) stack lies between the one of ITO and crystalline silicon, thus giving a smoother index transition than a direct ITO/a-Si/c-Si interface.

IV. Conclusion

A passivating electron contact based on a buffer SiO_X supported by a highly phosphorus-doped bilayer structure of silicon phases embedded in a silicon oxide matrix has been analyzed. The influence of doping concentration in the deposited layer and the subsequent annealing dwell time at 900 °C was related to the junction properties. The results indicate a tradeoff between reduction of the minority carriers, Auger recombination, and defect creation in the interfacial oxide. Based on EDNA 2 simulations, we discussed the impact of the doping profile on the relation between the emitter saturation current density J_0 and the SRV. The contact presented here exhibits a very similar dependence of SRV on phosphorus surface concentration as for passivation with dielectric layers reported in the literature. A deeper profile with a higher phosphorus concentration is less sensitive to the SRV and relies therefore less on chemical passivation of the interface. When using hydrogenation to optimize surface passivation, it should be kept in mind that the negative influence of the ITO sputtering (causing surface passivation damage) may be stronger in case of a predominant chemical passivation. For our sputtering conditions, we find a J_0 value of 12.1 fA cm^{-2} for higher doping levels and we note that such P doping levels are also needed in our mixed-phase SiO_X contacts to ensure a sufficient carrier transport through the layer. Finally, we presented a *planar* proof-of-concept solar cell with an *FF* of 79.4%, a J_{SC} of 33.9 mA cm^{-2} and a V_{OC} of 691 mV leading to a conversion efficiency of 18.6%. This result points out that using such high doping levels the current can be extracted efficiently while the mixed-phase SiO_X layer allows at the same time for a comparatively high short-circuit current density for flat cells due to a low level of parasitic absorption in the mixed-phase front layer stack.

References

[1] A. Cuevas, "Physical model of back line-contact front-junction solar cells," *J. Appl. Phys.*, vol. 113, no. 16, 2013, Art. no. 164502. [Online]. Available: https://doi.org/10.1063/1.4800840

[2] J. Y. Gan and R. M. Swanson, "Polysilicon emitters for silicon concentrator solar cells," in *Proc. Conf. Rec. 21st IEEE Photovolt. Spec. Conf.*, 1990, pp. 245–250. [Online]. Available: https://doi.org/10.1109/PVSC.1990.111625

[3] Y. H. Kwark, R. Sinton, and R. M. Swanson, "SIPOS Heterojunction contacts to silicon," vol. 94305, no. 415, pp. 742–745, 1984. [Online]. Available: https://doi.org/10.1109/IEDM.1984.190832

[4] E. Yablonovitch, T. Gmitter, R. M. Swanson, and Y. H. Kwark, "A 720 mV open circuit voltage SiOx:c-Si:SiOx double heterostructure solar cell," *Appl. Phys. Lett.*, vol. 47, no. 11, pp. 1211–1213, 1985. [Online]. Available: https://doi.org/10.1063/1.96331

[5] T. Matsushita, H. Hayashi, O.-U. Norikazu, and H. Hisayoshi, "A SIPOS-Si heterojunction transistor," *Jpn. J. Appl. Phys.*, vol. 20, pp. 75–81, 1981. [Online]. Available: https://doi.org/10.7567/JJAPS.20S1.75

[6] F. Feldmann, C. Reichel, and M. Hermle, "Si solar cells with top / rear poly-Si contacts," in *Proc. IEEE 43rd Photovolt. Spec. Conf.*, 2016, pp. 2421–2424. [Online]. Available: https://doi.org/10.1109/PVSC.2016.7750076

[7] U. Römer *et al.*, "Recombination behavior and contact resistance of n+ and p+ poly-crystalline Si/mono-crystalline Si junctions," *Sol. Energy Mater. Sol. Cells*, vol. 131, pp. 85–91, 2014. [Online]. Available: https://doi.org/10.1016/j.solmat.2014.06.003

[8] Y. Tao *et al.*, "730 mV implied Voc enabled by tunnel oxide passivated contact with PECVD grown and crystallized n+ polycrystalline Si," in *Proc. 2015 IEEE 42nd Photovolt. Spec. Conf.*, 2015, pp. 1–5. [Online]. Available: https://doi.org/10.1109/PVSC.2015.7356218

[9] D. L. Young *et al.*, "Carrier-selective, passivated contacts for high efficiency silicon solar cells based on transparent conducting oxides," in *Proc. 2014 IEEE 40th Photovolt. Spec. Conf.*, 2014, pp. 1–5. [Online]. Available: https://doi.org/10.1109/PVSC.2014.6925147

[10] G. Nogay *et al.*, "Interplay of annealing temperature and doping in hole selective rear contacts based on silicon-rich silicon-carbide thin films," *Sol. Energy Mater. Sol. Cells*, vol. 173, pp. 18–24, 2017. [Online]. Available: https://doi.org/10.1016/j.solmat.2017.06.039

This article has been accepted for inclusion in a future issue of this journal. Content is final as presented, with the exception of pagination.

[11] A. Richter *et al.*, “n-Type Si solar cells with passivating electron contact: Identifying sources for efficiency limitations by wafer thickness and resistivity variation,” *Sol. Energy Mater. Sol. Cells*, vol. 173, pp. 96–105, Dec. 2017. [Online]. Available: https://doi.org/10.1016/j.solmat.2017.05.042

[12] J. Krügener *et al.*, “Improvement of the SRH bulk lifetime upon formation of n-type POLO junctions for 25% efficient Si solar cells,” *Sol. Energy Mater. Sol. Cells*, vol. 173, pp. 85–91, Dec. 2017. [Online]. Available: https://doi.org/10.1016/j.solmat.2017.05.055

[13] R. Brendel and R. Peibst, “Contact selectivity and efficiency in crystalline silicon photovoltaics,” *IEEE J. Photovolt.*, vol. 6, no. 6, pp. 1413–1420, Nov. 2016. [Online]. Available: https://doi.org/10.1109/JPHOTOV.2016.2598267

[14] A. Stesmans, “Dissociation kinetics of hydrogen-passivated Pb defects at the (111)Si/SiO2 interface,” *Phys. Rev. B*, vol. 61, no. 12, pp. 8393–8403, 2000. [Online]. Available: https://doi.org/10.1103/PhysRevB.61.8393

[15] S. W. Glunz *et al.*, “The irresistible charm of a simple current flow pattern - 25% with a solar cell featuring a full area back contact,” in *Proc. 31st Eur. Photovolt. Sol. Energy Conf. Exhib.*, 2015, pp. 259–263. [Online]. Available: https://doi.org/10.4229/EUPVSEC20152015-2BP.1.1

[16] J. Stuckelberger *et al.*, “Passivating electron contact based on highly crystalline nanostructured silicon oxide layers for silicon solar cells,” *Sol. Energy Mater. Sol. Cells*, vol. 158, pp. 2–10, 2016. [Online]. Available: https://doi.org/10.1016/j.solmat.2016.06.040

[17] P. Cuony *et al.*, “Silicon filaments in silicon oxide for next-generation photovoltaics,” *Adv. Mater.*, vol. 24, no. 9, pp. 1182–1186, 2012. [Online]. Available: https://doi.org/10.1002/adma.201104578

[18] J. del Alamo, S. Swirhun, and R. M. Swanson, “Measuring and modeling minority carrier transport in heavily doped silicon,” *Solid State Electron.*, vol. 28, nos. 1/2, pp. 47–54, 1985. [Online]. Available: https://doi.org/10.1016/0038-1101(85)90209-6

[19] R. R. King, R. A. Sinton, and R. M. Swanson, “Studies of diffused phosphorus emitters: saturation current, surface recombination velocity, and quantum efficiency,” *IEEE Trans. Electron Devices*, vol. 37, no. 2, pp. 365–371, Feb. 1990. [Online]. Available: https://doi.org/10.1109/16.46368

[20] A. Cuevas, P. A. Basore, G. Giroult-Matlakowski, and C. Dubois, “Surface recombination velocity of highly doped n-type silicon,” *J. Appl. Phys.*, vol. 80, no. 6, pp. 3370–3375, 1996. [Online]. Available: https://doi.org/10.1063/1.363250

[21] J. Dziewior and W. Schmid, “Auger coefficients for highly doped and highly excited silicon,” *Appl. Phys. Lett.*, vol. 31, no. 5, pp. 346–348, Sep. 1977. [Online]. Available: https://doi.org/10.1063/1.89694

[22] A. Cuevas and D. Yan, “Misconceptions and misnomers in solar cells,” *IEEE J. Photovolt.*, vol. 3, no. 2, pp. 916–923, Apr. 2013. [Online]. Available: https://doi.org/10.1109/JPHOTOV.2013.2238289

[23] T. Yamamoto, “Bias temperature instability in scaled p+ polysilicon gate p-MOSFET’s,” *IEEE Trans. Electron Devices*, vol. 46, no. 5, pp. 921–926, May 1999. [Online]. Available: https://doi.org/10.1109/16.760398

[24] H. Kobayashi Asuha, O. Maida, M. Takahashi, and H. Iwasa, “Nitric acid oxidation of Si to form ultrathin silicon dioxide layers with a low leakage current density,” *J. Appl. Phys.*, vol. 94, no. 11, pp. 7328–7335, 2003. [Online]. Available: https://doi.org/10.1063/1.1621720

[25] Asuha *et al.*, “Ultrathin silicon dioxide layers with a low leakage current density formed by chemical oxidation of Si,” *Appl. Phys. Lett.*, vol. 81, no. 18, pp. 3410–3412, 2002. [Online]. Available: https://doi.org/10.1063/1.1517723

[26] A. Kimmerle, J. Greulich, and A. Wolf, “Carrier-diffusion corrected J0-analysis of charge carrier lifetime measurements for increased consistency,” *Sol. Energy Mater. Sol. Cells*, vol. 142, pp. 116–122, 2015. [Online]. Available: https://doi.org/10.1016/j.solmat.2015.06.043

[27] PVLighthouse, “EDNA2,” 2017. [Online]. Available: https://www2.pvlighthouse.com.au/calculators

[28] G. Nogay *et al.*, “Silicon-Rich silicon carbide hole-selective rear contacts for crystalline-silicon-based solar cells,” *ACS Appl. Mater. Interfaces*, vol. 8, no. 51, pp. 35660–35667, 2016. [Online]. Available: https://doi.org/10.1021/acsami.6b12714

[29] G. Nogay *et al.*, “Nanocrystalline silicon carrier collectors for silicon heterojunction solar cells and impact on low-temperature device characteristics,” *IEEE J. Photovolt.*, vol. 6, no. 6, pp. 1654–1662, Nov. 2016. [Online]. Available: https://doi.org/10.1109/JPHOTOV.2016.2604574

[30] E. Centurioni and D. Iencinella, “Role of front contact work function on amorphous silicon/crystalline silicon heterojunction solar cell performance,” *IEEE Electron Device Lett.*, vol. 24, no. 3, pp. 177–179, Mar. 2003. [Online]. Available: https://doi.org/10.1109/LED.2003.811405

[31] S. P. Harvey, T. O. Mason, Y. Gassenbauer, R. Schafranek, and A. Klein, “Surface versus bulk electronic/defect structures of transparent conducting oxides: I. Indium oxide and ITO,” *J. Phys. D. Appl. Phys.*, vol. 39, no. 18, pp. 3959–3968, 2006. [Online]. Available: https://doi.org/10.1088/0022-3727/39/18/006

[32] D. K. Schroder and D. L. Meier, “Solar cell contact resistance - A review,” *IEEE Trans. Electron Devices*, vol. ED-31, no. 5, pp. 637–647, May 1984. [Online]. Available: https://doi.org/10.1109/T-ED.1984.21583

[33] A. Klein *et al.*, “Transparent conducting oxides for photovoltaics: Manipulation of fermi level,work function and energy band alignment,” *Mater. (Basel)*, vol. 3, no. 11, pp. 4892–4914, 2010. [Online]. Available: https://doi.org/10.3390/ma3114892

[34] T. Trupke *et al.*, “Temperature dependence of the radiative recombination coefficient of intrinsic crystalline silicon,” *J. Appl. Phys.*, vol. 94, no. 8, pp. 4930–4937, 2003. [Online]. Available: https://doi.org/10.1063/1.1610231

[35] A. Richter, S. W. Glunz, F. Werner, J. Schmidt, and A. Cuevas, “Improved quantitative description of Auger recombination in crystalline silicon,” *Phys. Rev. B*, vol. 86, no. 16, pp. 1–14, 2012. [Online]. Available: https://doi.org/10.1103/PhysRevB.86.165202

[36] S. Solmi *et al.*, “Dopant and carrier concentration in Si in equilibrium with monoclinic SiP precipitates,” *Phys. Rev. B*, vol. 53, no. 12, pp. 7836–7841, 1996. [Online]. Available: https://doi.org/10.1103/PhysRevB.53.7836

[37] A. Kimmerle *et al.*, “Precise parameterization of the recombination velocity at passivated phosphorus doped surfaces,” *J. Appl. Phys.*, vol. 119, no. 2, 2016, Art. no. 025706. [Online]. Available: https://doi.org/10.1063/1.4939960

[38] S. W. Glunz *et al.*, “Emitter dark saturation currents of high-efficiency solar cells with inverted pyramids,” in *Proc. 13th Eur. Photovolt. Sol. Energy Conf.*, 1995, pp. 409–412.

[39] M. J. Kerr, J. Schmidt, A. Cuevas, and J. H. Bultman, “Surface recombination velocity of phosphorus-diffused silicon solar cell emitters passivated with plasma enhanced chemical vapor deposited silicon nitride and thermal silicon oxide,” *J. Appl. Phys.*, vol. 89, no. 7, pp. 3821–3826, 2001. [Online]. Available: https://doi.org/10.1063/1.1350633

[40] P. P. Altermatt *et al.*, “Numerical modeling of highly doped Si:P emitters based on Fermi-Dirac statistics and self-consistent material parameters,” *J. Appl. Phys.*, vol. 92, no. 6, pp. 3187–3197, 2002. [Online]. Available: https://doi.org/10.1063/1.1501743

[41] M. Morales-Masis, S. Martin De Nicolas, J. Holovsky, S. De Wolf, and C. Ballif, “Low-temperature high-mobility amorphous IZO for silicon heterojunction solar cells,” *IEEE J. Photovolt.*, vol. 5, no. 5, pp. 1340–1347, Sep. 2015. [Online]. Available: https://doi.org/10.1109/JPHOTOV.2015.2450993.

[42] S. De Wolf, A. Descoeudres, Z. C. Holman, and C. Ballif, “High-efficiency silicon heterojunction solar cells: A review,” *Green*, vol. 2, no. 1, pp. 7–24, 2012. [Online]. Available: https://doi.org/10.1515/green-2011-0039.

[43] A. Tomasi *et al.*, “Transparent electrodes in silicon heterojunction solar cells: influence on contact passivation,” *IEEE J. Photovolt.*, vol. 6, no. 1, pp. 17–27, Jan. 2016. [Online]. Available: https://doi.org/10.1109/JPHOTOV.2015.2484962

[44] R. Rössler, C. Leendertz, L. Korte, N. Mingirulli, and B. Rech, “Impact of the transparent conductive oxide work function on injection-dependent a-Si:H/c-Si band bending and solar cell parameters,” *J. Appl. Phys.*, vol. 113, no. 14, 2013, Art. no. 144513. [Online]. Available: https://doi.org/10.1063/1.4799042

[45] M. Wolf and H. Rauschenbach, “Series resistance effects on solar cell measurements,” *Adv. Energy Convers.*, vol. 3, no. 2, pp. 455–479, 1963. [Online]. Available: https://doi.org/10.1016/0365-1789(63)90063-8

[46] D. Pysch, A. Mette, and S. W. Glunz, “A review and comparison of different methods to determine the series resistance of solar cells,” *Sol. Energy Mater. Sol. Cells*, vol. 91, no. 18, pp. 1698–1706, 2007. [Online]. Available: https://doi.org/10.1016/j.solmat.2007.05.026

[47] PVLighthouse, “Wafer ray tracer,” 2017. [Online]. Available: https://www2.pvlighthouse.com.au/calculators/wafer ray tracer/wafer ray tracer.html

Authors’ photographs and biographies not available at the time of publication.